

An iterative technique to segment PET lesions using a Monte Carlo based mathematical model

S. A. Nehmeh^{a)}

Department of Medical Physics, Memorial Sloan-Kettering Cancer Center, New York, New York 10021

H. El-Zeftawy

Cardiology Associates, Woonsocket, Rhode Island 02895

C. Greco

Department of Radiation Oncology, Memorial Sloan-Kettering Cancer Center, New York, New York 10021

J. Schwartz, Y. E. Erdi, A. Kirov, and C. R. Schmidlein

Department of Medical Physics, Memorial Sloan-Kettering Cancer Center, New York, New York 10021

A. B. Gyau and S. M. Larson

Department of Radiology, Memorial Sloan-Kettering Cancer Center, New York, New York 10021

J. L. Humm

Department of Medical Physics, Memorial Sloan-Kettering Cancer Center, New York, New York 10021

(Received 4 March 2009; revised 14 August 2009; accepted for publication 15 August 2009; published 24 September 2009)

Purpose: The need for an accurate lesion segmentation tool in ^{18}F FDG PET is a prerequisite for the estimation of lesion response to therapy, for radionuclide dosimetry, and for the application of ^{18}F FDG PET to radiotherapy planning. In this work, the authors have developed an iterative method based on a mathematical fit deduced from Monte Carlo simulations to estimate tumor segmentation thresholds.

Methods: The GATE software, a GEANT4 based Monte Carlo tool, was used to model the GE Advance PET scanner geometry. Spheres ranging between 1 and 6 cm in diameters were simulated in a 10 cm high and 11 cm in diameter cylinder. The spheres were filled with water-equivalent density and simulated in both water and lung equivalent background. The simulations were performed with an infinite, 8/1, and 4/1 target-to-background ratio (T/B). A mathematical fit describing the correlation between the lesion volume and the corresponding optimum threshold value was then deduced through analysis of the reconstructed images. An iterative method, based on this mathematical fit, was developed to determine the optimum threshold value. The effects of the lesion volume and T/B on the threshold value were investigated. This method was evaluated experimentally using the NEMA NU2-2001 IEC phantom, the ACNP cardiac phantom, a randomly deformed aluminum can, and a spheroidal shape phantom implemented artificially in the lung, liver, and brain of patient PET images. Clinically, the algorithm was evaluated in six lesions from five patients. Clinical results were compared to CT volumes.

Results: This mathematical fit predicts an existing relationship between the PET lesion size and the percent of maximum activity concentration within the target volume (or threshold). It also showed a dependence of the threshold value on the T/B, which could be eliminated by background subtraction. In the phantom studies, the volumes of the segmented PET targets in the PET images were within 10% of the nominal ones. Clinically, the PET target volumes were also within 10% of those measured from CT images.

Conclusions: This iterative algorithm enabled accurately segment PET lesions, independently of their contrast value. © 2009 American Association of Physicists in Medicine.

[DOI: [10.1118/1.3222732](https://doi.org/10.1118/1.3222732)]

Key words: PET, lesion segmentation, threshold

I. INTRODUCTION

^{18}F FDG PET, a quantitative imaging modality, may now be considered as one of the most accurate imaging techniques for diagnosis, staging, and post-treatment restaging of various cancers.¹⁻⁶ The tumor detection is based on the increased metabolism of glucose in viable malignant cells. A radiotracer uptake of an $\text{SUV} > 2.5$ (using filtered back projec-

tion reconstruction) has been reported to be an indicator of higher probability of malignancy.⁷ The final assessment of the status of the disease is made by assessing this SUV value in combination with, among other indicators, the lesion size.⁸ Therefore, having accurately determined lesion boundaries is an important prerequisite for the effective use of PET, particularly in radiation therapy planning. Furthermore, precise knowledge on lesion mass, thus volume, is necessary when

performing dosimetry for tumor targeting agents such as ^{124}I for thyroid cancer⁹ or radiolabeled peptides and antibodies.^{10–12} In many institutions, anatomic (CT) and metabolic (PET) information is routinely combined to determine the planning target volume^{13–18} for radiotherapy. Finally, the use of PET is increasingly being explored as an alternative to anatomical imaging modalities for the evaluation of cancer treatment response. For example, Larson *et al.* proposed a new parameter, total lesion glycolysis, as a quantitative measure of tumor response to treatment. This method combines changes in lesion activity, i.e., FDG uptake, with the tumor volume.¹⁹

Several techniques have been developed to estimate the volume of a lesion from PET images. The method that is being used the most is based on the visual interpretation of the PET scan and the definition of contours as judged by the experienced nuclear medicine physician.²⁰ In a study, an SUV of 2.5 was suggested to delineate the gross target volume (GTV) from the surrounding.²¹ On another hand, Erdi *et al.* estimated lesion size by using a fixed intensity threshold value which they determined from phantom measurements.²² They showed that the threshold value (defined as a percentage of the maximum lesion intensity) at which the real volume of the spheres was obtained is inversely correlated with the lesion volume and to the target-to-background ratio (T/B). Moreover, by fitting the data to a mixed exponential model, they determined the asymptotic relationship between threshold and volume for a given T/B for lesion volumes greater than 4 cc. This asymptotic, thus fixed threshold for a given T/B, was then used to determine patient lesion volumes and was in good agreement with CT measurements.²² For small lesions smaller than 4 cc, however, significant discrepancies were observed, which may have been due to the nonlinearity of the PET system (characterized by the partial volume effect) for target sizes smaller than $2 \times \text{FWHM}$ of the spatial resolution of the camera. Black *et al.* suggested that the FDG PET lesion volume can be described using a threshold SUV according to the regressive function (threshold $\text{SUV} = 0.307 \times \text{mean target SUV} + 0.588$).²³ Unlike Erdi, Black *et al.* showed that the threshold SUV is inversely proportional to the target volume and background activity concentration.²³ In a more recent study, El-Bassiouni *et al.* proposed that a patient specific threshold may be optimal.²⁴ The authors used CT as a guideline for defining the PET threshold value. They also identified that the fixed threshold values appropriate for targets with maximum activity concentration (after background subtraction) greater than 30 kBq/ml was 20%, and for those smaller or equal to 30 kBq/ml it was 40%.

In the majority of the thresholding techniques that were developed, investigators showed that the threshold value depends on the T/B or contrast.^{22,23,25} Soma *et al.* showed that a T/B based thresholding technique may be more accurate than using a fixed threshold method,²⁵ as it was suggested by Erdi *et al.*²² The same group also suggested that the different tracer uptake in the tumor surrounding tissues has to be considered.²⁵

In this study, we developed a mathematical tool using results of Monte Carlo simulations from which we determined the dependence of the threshold value on the target size, contrast, and maximum activity concentration of FDG-PET target volumes in 3D PET acquisitions. The model was evaluated with both experimental phantom and patient data. Tumor volumes were then compared to CT volumes.

II. METHODS AND MATERIALS

II.A. Monte Carlo simulations

II.A.1. Monte Carlo tool

The GEANT4 Application for tomographic emission (GATE) package²⁶ was used to model the GE Advance PET scanner geometry.²⁷ GATE was developed by a multi-institutional consortium that uses GEANT4 to model and simulate the physics of medical nuclear imaging, in particular physics of PET and SPECT. GEANT4 is a toolkit for simulating the transport of particles through matter. This toolkit has a wide range functionality, which includes particle tracking, geometry, physics models, and particle hits. GEANT4 is used in applications encompassing particle physics, nuclear physics, particle-accelerator physics, space engineering, and medical physics.

II.A.2. Monte Carlo simulated phantom studies

A cylindrical phantom 11 cm in diameter and 10 cm in height was simulated using the Monte Carlo code described in Sec. II A 1. The simulated phantom was filled with material of either lung tissue or water (to simulate other normal tissues)-equivalent density. In addition, spheres were simulated at the center of this phantom, with their diameters ranging from 1.0 cm ($\sim 2 \times \text{FWHM}$ for the GE Advance) to 6.0 cm in increment of 0.5 cm. All spheres had a 1 mm thick plastic-equivalent density wall. The spheres were simulated as being filled with water-equivalent density.

To be able to determine the SUV threshold values that would lead to a correct determination of accurate lesion volumes, it is first necessary to investigate the relationship and correlation between volume and threshold. In what follows, we always define threshold as a given percentage of the maximum activity concentration within the volume of interest. This same approach was taken to investigate the effect of the lesion contrast and maximum activity concentration on the determination of an appropriate threshold. Three types of simulations were performed in order to answer these questions. For these simulations, lesions were placed within tissues with a variety of lesion contrasts as observed clinically.

II.A.2.a. Lung lesions. Lung tissue has a lower density than any other tissues in the body. In addition, lesions in the lung have an average T/B of 8:1 and activity concentration of $1 \mu\text{Ci/cc}$. Thus, the simulated lesions (represented as spheres with radii as described above) were filled with $1 \mu\text{Ci/cc}$ of ^{18}F and placed within a lung-equivalent density background with T/B:8/1. This setup was also simulated with no background activity for comparison.

II.A.2.b. Liver lesions. Liver tissue has a density approximately equal to that of water and other soft tissues except

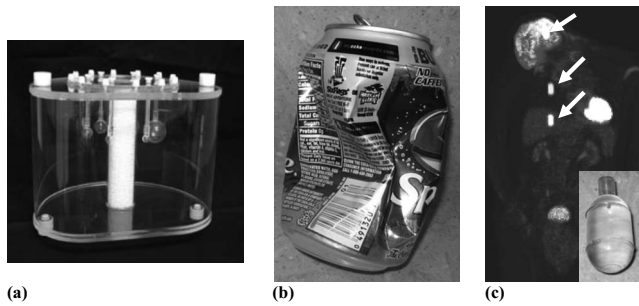


FIG. 1. The three phantoms: (a) NEMA2001 IEC, (b) deformed aluminum can, and coronal view of a patient showing the implemented spheroid in the brain, lung, and liver are shown.

lung. Generally, liver lesions are observed with T/B:4/1. We chose to simulate the liver for these reasons and used, once more, the Monte Carlo geometry described above, simulating the spheres with $1 \mu\text{Ci}/\text{cc}$ of ^{18}F and with T/B:4/1. The background was simulated with water-equivalent density.

II.A.2.c. Effect of target activity concentration. The goal of this simulation was to investigate the effect of the target activity concentration on its corresponding threshold value. For this purpose, MC simulation for a 3 cm diameter sphere simulated in water-equivalent background and with infinite T/B was performed. The simulation was repeated for four activity concentrations in the sphere: 0.5, 1.0, 1.5, and $2.0 \mu\text{Ci}/\text{cc}$.

II.B. Experimental data

II.B.1. Phantom I

The National Electrical Manufacturers Association (NEMA) 2001 IEC phantom [Fig. 1(a)], with six spheres ranging between 10 and 37 mm (± 1 mm) in diameters, was used to evaluate the lesion segmentation technique described in this manuscript. The spheres were filled with $1.0 \mu\text{Ci}/\text{cc}$ ^{18}F FDG, with a \sim T/B:10/1. The phantom was scanned for 15 min [in single field of view (FOV)] in 3D mode to reduce the effect of statistical fluctuation. Data were acquired on the GE Discovery LS PET/CT (GE Healthcare Technologies, Waukesha, WI) scanner. The PET images were reconstructed using the 3D FBP algorithm provided by the manufacturer.

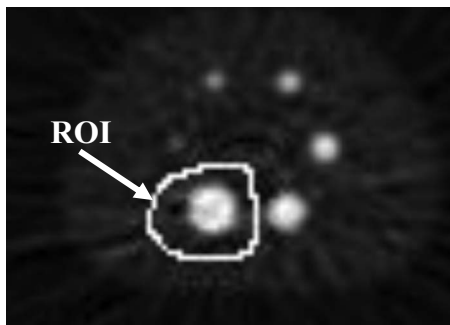


FIG. 2. Example of how the ROI would be drawn around the target. The pixel values included inside the ROI are exported to an output file, which will be the input to the segmentation algorithm. The background included in the ROI is used to estimate the background level in the corresponding slice.

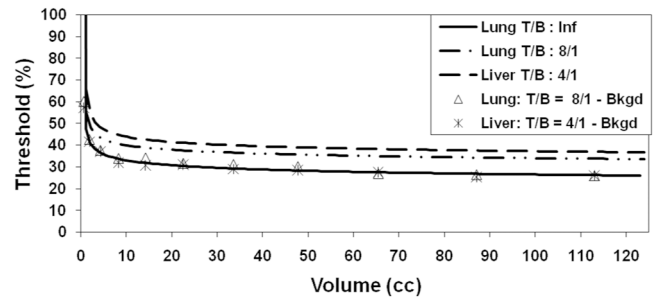


FIG. 3. The threshold values versus spheres volumes for infinite, 8/1, and 4/1 T/Bs are shown. This figure also shows the data from T/Bs of 8/1 and 4/1 after background subtraction. After background subtraction, those data sets (T/B < infinity) were in good agreement with the cold background distribution. This enabled eliminate the dependence of the threshold values on the T/B when subtracting the background.

II.B.2. Phantom II

The shape of the lesion may have an effect on the accuracy of our segmentation tool in correctly estimating the lesion volume. In order to address this question, we did two separate phantom scans. First, the ACNP cardiac phantom was filled with ~ 195.1 cc of $1 \mu\text{Ci}/\text{cc}$ ^{18}F FDG and scanned for 15 min. For the second scan, we used an aluminum can which we deformed [Fig. 1(b)] and filled with 115 cc of $1 \mu\text{Ci}/\text{cc}$ ^{18}F FDG. This was also scanned for 15 min.

II.B.3. Phantom III

A 10.5 cc capsule, filled with $1 \mu\text{Ci}/\text{cc}$ of ^{18}F FDG, was scanned in air for 15 min. The capsule image was then digitally merged over the lung, liver, and brain PET images of a patient [Fig. 1(c)].

II.B.4. Patient data

Six lesions from five patients were included in this study and used to evaluate the segmentation algorithm. All data were acquired in 3D mode on the GE Discovery LS PET/CT scanner and then reconstructed using the FBP reconstruction

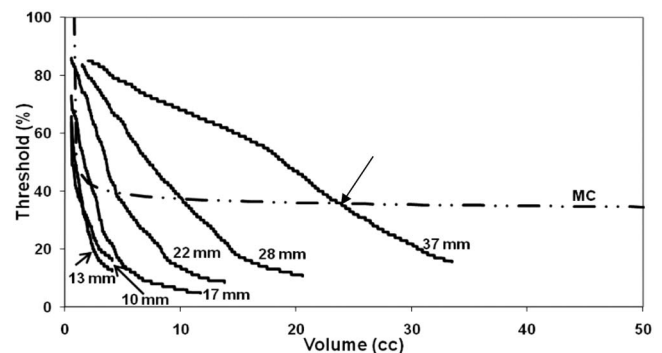


FIG. 4. Behavior of the Thr_{\min} versus V_{nominal} for the six spheres of the IEC phantom, as the algorithm iterates over both the threshold and volume. Each of the distributions is labeled with the corresponding sphere diameter. As an example, the arrow points to the point of intersection with the MC model for the 37 mm diameter sphere, which corresponds to the optimum threshold and volume for the target in question.

algorithm provided by the manufacturer. Lesion volumes were contoured on CT images by a radiologist and considered as the gold standard.

II.C. Sinogram binning and image reconstruction

The sinograms generated by the Monte Carlo simulations were binned according to the GE Advance 3D acquisition format. The sinograms were corrected for attenuation and then reconstructed with 3D filtered backprojection algorithm using the software for tomographic image reconstruction (STIR).^{28,29}

All PET images, whether resulting from experimental or simulated scans, or from patient studies, were reconstructed in a 128×128 matrix and a 50 cm FOV (i.e., voxel dimensions of $3.9 \times 3.9 \times 4.25$ mm³).

III. ANALYSIS

The development of a tool that can be applied to provide the optimal threshold for patient lesions requires the use of MC simulations in order to first determine an empirical mathematical model capable of predicting the appropriate threshold as a function of the lesion volume.

Once MC data are obtained, finding suitable thresholds for the MC data is the necessary next step. This must be done “by hand” with the *a priori* knowledge on the relevant volumes, which are known exactly since they were required inputs for the simulation. Once this task was completed, the empirical model was determined by least-squares fitting techniques and tested with phantom and clinical data. The analysis below describes the threshold and background subtraction steps, which result in the data, threshold as a function of volume. The procedure for fitting these data and determine the appropriate equation is then described.

III.A. Threshold estimation

The lesion contours were drawn using the IMAGEJ software³⁰ on a slice-by-slice basis. In each slice, the region of interest (ROI) was drawn so as to include some of the background, while excluding any neighboring regions of high uptake (Fig. 2). The voxel coordinates and intensities of the pixels in each of these ROIs were then written to output files. The background was estimated individually for each transaxial slice as described below and then subtracted from each voxel on a slice-by-slice basis.

The target volume was defined as the volume occupied by those voxels whose intensities were greater than a predefined threshold. A threshold is defined as a given percent of the maximum activity concentration value within the target volume. The threshold values (resulting in the correct lesions volumes) determined for the images obtained from the Monte Carlo simulations were plotted versus the lesions volumes, and model fitting the data was found (Fig. 3). The value of the threshold that would result in the correct target volume was determined using the following steps:

(a) A threshold value was chosen from 0% to 100% of the maximum activity concentration in increments of 1%.

(b) For each value of the threshold, the target volume was calculated by counting the total number of voxels with intensity satisfying the threshold criterion multiplied by the voxel volume. The target volume was then compared to the theoretical target volume which was determined by evaluating the best-fit MC function at this threshold level. The percent difference between target and theoretical volumes [%diff(*V*)] was calculated for each threshold value.

(c) The threshold (Thr_{\min}) corresponding to the target volume which had the smallest percent difference [%diff(*V*)] was taken as the real lesion volume. The results from the six spheres of the IEC phantom are shown in Fig. 4. As an example, the arrow points to the (V_{optimum} , $\text{Thr}_{\text{optimum}}$) point for the 37 m diameter sphere.

III.B. Background subtraction

It is important to exclude the target volume from the volume of interest used to estimate the background. On the other hand, if the above segmentation technique was performed with the assumption of a cold background, the target volume would then be overestimated (compared to the correct volume). Thus, to estimate the background, the above segmentation procedure was run twice. First, a cold background was assumed. This results in overestimating the actual target size. All the voxels lying outside this estimated target volume which are also still within the ROI are then used to estimate the background. The average intensity of these background voxels is then calculated and subtracted. This procedure was performed on a slice-by-slice basis. Then, a second run of the segmentation procedure is done on the background-subtracted ROI to accurately determine the lesion volume.

III.C. Empirical model

Figure 3 shows a plot of the threshold as a function of the MC simulated lesion volume for the cases of both lung (T/B: 8/1) and liver (T/B: 4/1), as well as for the case of a cold background. A mathematical model was determined using the CURVEEXPERT (Ref. 31) software, which provides the option to automate the search for an optimal fitting function for the available data. This is especially useful when searching for a mathematical model empirically because it is not possible to derive one from first principles. The CURVEEXPERT program compares the data to each model in its database and chooses the best curve among the fits. This automated procedure was used to perform least-squares fit on the data set corresponding to the MC lung data with no background, described in Sec. II B 1. The resulting best-fit model was of the form presented in Eq. (1), where a_0 , a , and b are the parameters to be determined by the regression,

$$\text{Threshold} (\%) = a_0 + \exp^{[a+(b/V)+c \log V]}. \quad (1)$$

The parameters resulting from the fit are

TABLE I. Threshold values for the 37 mm diameter sphere simulated with different activity concentrations.

Act. Conc. ($\mu\text{Ci/cc}$)	Threshold (%)
0.5	38
1	40
1.5	41.5
2	39.5

$$a_0 = 5, \quad a = 3.568, \quad b = 0.197, \quad c = -0.1069.$$

The fit correlation r was 0.98. These results revealed a dependence of the threshold on T/B. The threshold appears to increase as the lesion contrast decreases. However, when background subtraction is performed for both the T/B=8/1 and T/B=4/1 cases, the optimum threshold values overlapped with the infinite contrast (cold background) curve.

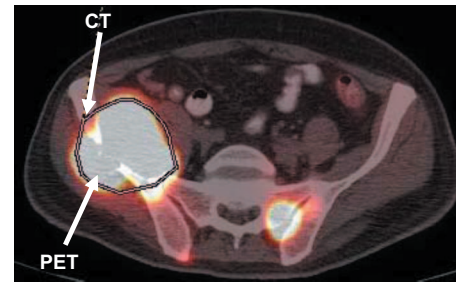
IV. RESULTS

Figure 3 shows the result of (1) the empirical fit and (2) the effectiveness of this model for all MC data sets regardless of T/B once background is subtracted. The MC simulations showed a fluctuation of about 4% in the threshold as a result of different target activity concentrations (Table I), which may be a consequence of statistical noise.

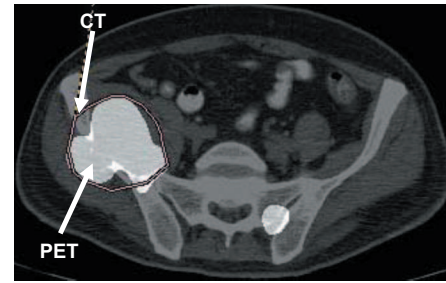
Figure 4 shows the (threshold, volume) point behavior, for each of the six spheres, as a result of the V_{target} -threshold iterations. The six curves, from right to left, correspond to the six spheres, respectively, from the largest to the smallest. The arrow points to the optimum threshold-volume point for the 37 mm sphere. In Fig. 5, the CT contour, which was drawn by the radiologist without looking at PET images, was copied to the fused PET/CT images. Figures 5(a) and 5(b) show the PET FDG distribution before and after applying the segmentation threshold for the slice of the largest lesion cross section. The PET lesion, defined by the thresholding

TABLE II. The nominal volumes for the six spheres of the NEMA 2001 IEC phantom, together with the measured volumes and the corresponding ESDs from the 3D PET images using the iterative method described in the manuscript are represented. The percent differences between the nominal and measured ESDs are also summarized.

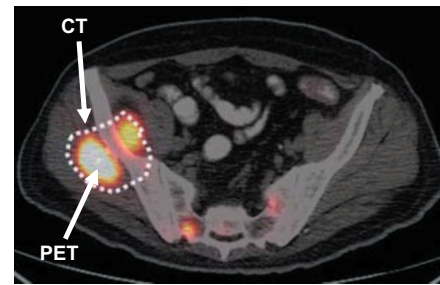
Phantom	V_{nominal}	V_{meas}	%error
Sphere	26.51	25.91	-2.26
Sphere	11.49	11.25	-2.07
Sphere	5.57	5.253	-5.73
Sphere	2.57	2.53	-1.6
Sphere	1.15	1.07	-3.93
Sphere	0.52	0.55	5.09
Cardiac	195.1	195.9	-0.41
Pepsi can	115	109.23	5.02
Capsule/air	10.5	10.15	-3.33
capsule/lung	10.5	9.61	-8.57
Capsule/liver	10.5	9.825	-6.43
Capsule/brain	10.5	9.91	-5.61



(a)



(b)



(c)

FIG. 5. (a) PET-CT fused image for the slice of the largest cross section of lesion 6. The CT contour, as it was drawn by the radiologist, without looking at PET images, is shown. The PET FDG distributions before (a) and after (b) applying the segmentation threshold are shown. The PET lesion, defined by the thresholding algorithm described in this study, appears to perfectly fit within the CT contour (b). (c) shows an example of discrepancies in the contoured areas in PET and CT, which contributed to the high percent difference between the PET and CT volumes. While no FDG uptake appeared in the iliac bone, CT contour incorporated those volumes.

algorithm described in this study, appears to perfectly fit within the CT contour [Fig. 5(b)]. However, a discrepancy in the contoured areas in PET and CT appears in the left posterior area of the lesion, which contributed to the high percent difference between the PET and CT volumes. Figure 5(c) shows another example of discrepancies between PET and CT volumes. While no FDG uptake appeared in the iliac bone, CT contour incorporated those volumes. Table II lists the nominal phantom volumes, together with those measured in the PET images. In Table III, the volumes of six lesions measured in both PET and CT are summarized. The percent errors between the PET and CT volumes are also reported.

V. DISCUSSION

An accurate, robust, and easily implemented lesion segmentation tool in PET has become a necessity for the con-

TABLE III. Summary of six lesion volumes measured from PET and CT images. PET volumes were segmented using the algorithm described in this work. CT volumes were contoured by a radiologist. The percent differences between the two measurements are also reported. The CT volumes are considered as the gold standard.

Patient	Lesion	Lesion site	VCT	V_{meas}	%error
1	1	Lung	334.67	318.32	4.89
2	2	Axilla	216.38	194.94	9.91
3	3	Lung	81.74	83.59	-2.26
	4	Lung	33.93	30.85	9.09
4	5	Lung	26.22	25.45	2.94
5	6	Iliac bone	176.63	110.37	37.53

sistent classification of lesion volumes from FDG scans. This is especially important with the growing emphasis on PET for the estimation of lesion response to therapy, for radionuclide dosimetry, and for the incorporation of FDG-PET information for in the delineation of target volume in radiotherapy planning. In this work, we have developed a simple analytical method to estimate tumor segmentation thresholds, determined from Monte Carlo simulations of different FDG configurations with lesions of different shapes and sizes. Our Monte Carlo based mathematical fit predicts an existing relationship between the PET target volume and the percent of maximum activity concentration within the target volume (i.e., threshold). Based on Monte Carlo simulations, we showed a dependence of the model on the lesion contrast, which can be effectively resolved by performing a background subtraction. We also observed that there was no significant dependence between the threshold value and the activity concentration within the target volume on the estimated optimum threshold values.

Our results were within 10% agreement with the nominal volumes, for both phantom and patients studies (but for patient 5), for which CT volumes were assumed the gold standard. For patient 5, visual inspection of CT contours and PET FDG distribution confirmed that the high percent difference between PET and CT segmented volumes was due to differences between the anatomical and metabolic lesion geometry. Uncertainties in the CT lesion contours may contribute to an increased uncertainty between the PET and the CT measured volumes in the clinical data sets. In a study that included eight patients, Steen *et al.* reported a CT-GTV change up to seven times due to intraobserver variability.³² Another major effect is the difference in the spatial resolution between CT and PET images. PET pixels are 16 times larger than CT ones, which may jeopardize the accuracy when determining the PET target boundaries. Our phantom results showed an increase in percent deviation from the nominal values for the spheroidal lesion that were artificially incorporated into the patient's PET images. Visual inspection of the registered lesion showed some distortion in the lesion shape, and thus its volume, possibly due to the interpolation between pixels during the registration process. This lesion segmentation method was not limited to regular lesion shapes (based on which the mathematical fit was derived). In

both the ACNP cardiac phantom and the deformed aluminum can experiments, the targets were accurately segmented to within 10%.

Extrapolation of the Erdi *et al.* mathematical fit to large lesion volumes resulted in increased errors as was discussed in their manuscript.²² This may be due to the limitation in the range of spherical volumes they included in their study. Consequently, it was necessary for them to terminate the regression at a threshold of 29% in the case of large lesions. Erdi *et al.* also mentioned that a 30% versus a 42% threshold did not show any major impact on their results²² for large lesion volumes. In this study, the mathematical fit yielded a more accurate description of the (threshold, lesion-volume) relationship at large lesion volumes. The threshold value decreases slowly for lesion volumes greater than 10 cc, which may suggest an acceptable approximation of the lesion volumes with a fixed threshold of ~31%, which corresponds to a volume of greater than 10 cc.

This algorithm was optimized for the GE Advance PET scanner. The model fit deduced from MC simulation depends on the scanner characteristics like resolution, pixel size, and recovery coefficients. Whether the same model can be used to segment lesions imaged on different PET scanners needs to be validated before it can be implemented. This would be the task for future work.

VI. CONCLUSIONS

In this study, we have developed a novel technique to estimate the PET target volumes, based on MC simulations, and an iterative method. The mathematical fit showed a strong correlation ($r=0.98$) between the lesion volume and the corresponding threshold value. Most importantly, this work also demonstrated that, after background subtraction, this correlation can be described by one set of fit parameters which incorporates lesion volumes, thus removing the influence of lesion contrast on the threshold parameters.

ACKNOWLEDGMENTS

The authors would like to thank Dr. C. Stearns and Dr. K. Thielemans from GE Health Care for their great support.

^{a)} Author to whom correspondence should be addressed. Electronic mail: nehmehs@mskcc.org; Present address: 1275 York Ave., New York, NY

10021. Telephone: 212-639-2175; Fax: 917-432-2379.
- ¹R. M. Pieterman *et al.*, "Preoperative staging of nonsmall-cell lung cancer with positron emission tomography," *N. Engl. J. Med.* **343**, 254–261 (2000).
 - ²B. A. Dwamena *et al.*, "Metastases from non-small cell lung cancer: Mediastinal staging in the 1990s—Meta-analytic comparison of PET and CT," *Radiology* **213**, 530–536 (1999).
 - ³V. Kalf *et al.*, "Clinical impact of (18)F fluorodeoxyglucose positron emission tomography in patients with non-small-cell lung cancer: A prospective study," *J. Clin. Oncol.* **19**, 111–118 (2001).
 - ⁴M. P. MacManus *et al.*, "F-18 fluorodeoxyglucose positron emission tomography staging in radical radiotherapy candidates with non-small cell lung carcinoma: Powerful correlation with survival and high impact on treatment," *Cancer* **92**, 886–895 (2001).
 - ⁵E. Salminen and M. MacManus, "Impact of FDG-labelled positron emission tomography imaging on the management of nonsmall-cell lung cancer," *Ann. Med.* **33**, 404–409 (2001).
 - ⁶K. Higashi *et al.*, "Value of whole-body FDG PET in the management of lung cancer," *Ann. Nucl. Med.* **17**, 1–14 (2001).
 - ⁷V. J. Lowe *et al.*, "Prospective investigation of positron emission tomography in lung nodules," *J. Clin. Oncol.* **16**, 1075–1084 (1998).
 - ⁸I. Brink *et al.*, "Increased metabolic activity in the thymus gland studied with ¹⁸F-FDG PET: Age dependency and frequency after chemotherapy," *J. Nucl. Med.* **42**, 591–595 (2001).
 - ⁹S. M. Eschmann, G. Reischl, K. Bilger, J. Kupferschläger, M. H. Thelen, B. M. Dohmen, H. Besenfelder, and R. Bares, "Evaluation of dosimetry of radioiodine therapy in benign and malignant thyroid disorders by means of iodine-124 and PET," *Eur. J. Nucl. Med. Mol. Imaging* **29**(6), 760–767 (2002).
 - ¹⁰M. K. Robinson, M. Doss, C. Shaller, D. Narayanan, J. D. Marks, L. P. Adler, D. E. Gonzalez Trotter, and G. P. Adams, "Quantitative immunopositron emission tomography imaging of HER2-positive tumor xenografts with an iodine-124 labeled anti-HER2 diabody," *Cancer Res.* **65**(4), 1471–1478 (2005).
 - ¹¹V. Kenanova, T. Olafsen, D. M. Crow, G. Sundaresan, M. Subbarayan, N. H. Carter, D. N. Ikle, P. J. Yazaki, A. F. Chatzioannou, S. S. Gambhir, L. E. Williams, J. E. Shively, D. Colcher, A. A. Raubitschek, and A. M. Wu, "Tailoring the pharmacokinetics and positron emission tomography imaging properties of anti-carcinoembryonic antigen single-chain Fv-Fc antibody fragments," *Cancer Res.* **65**(2), 622–631 (2005).
 - ¹²F. Daghighian, K. S. Pentlow, S. M. Larson, M. C. Graham, G. R. DiResta, S. D. Yeh, H. Macapinlac, R. D. Finn, E. Arbit, and N. K. Cheung, "Development of a method to measure kinetics of radiolabelled monoclonal antibody in human tumour with applications to icrodosimetry: Positron emission tomography studies of iodine-124 labelled 3F8 monoclonal antibody in glioma," *Eur. J. Nucl. Med.* **20**(5), 402–409 (1993).
 - ¹³P. Bowden *et al.*, "Measurement of lung tumor volumes using three-dimensional computer planning software," *Int. J. Radiat. Oncol., Biol., Phys.* **53**, 566–573 (2002).
 - ¹⁴K. Mah *et al.*, "The impact of (18)FDGPET on target and critical organs in CT-based treatment planning of patients with poorly defined non-small-cell lung carcinoma: A prospective study," *Int. J. Radiat. Oncol., Biol., Phys.* **52**, 339–350 (2002).
 - ¹⁵P. Giraud *et al.*, "CT and (18)Fdeoxyglucose (FDG) image fusion for optimization of conformal radiotherapy of lung cancers," *Int. J. Radiat. Oncol., Biol., Phys.* **49**, 1249–1257 (2001).
 - ¹⁶C. A. Perez *et al.*, "Functional imaging in treatment planning in radiation therapy: A review," *Rays* **27**, 157–173 (2002).
 - ¹⁷C. B. Caldwell *et al.*, "Can PET provide the 3D extent of tumor motion for individualized internal target volumes? A phantom study of the limitations of CT and the promise of PET," *Int. J. Radiat. Oncol., Biol., Phys.* **55**, 1381–1393 (2003).
 - ¹⁸Y. E. Erdi *et al.*, "Radiotherapy treatment planning for patients with non-small cell lung cancer using positron emission tomography (PET)," *Radiother. Oncol.* **62**, 51–60 (2002).
 - ¹⁹S. M. Larson, Y. Erdi, T. Akhurst, M. Mazumdar, H. A. Macapinlac, R. D. Finn, C. Casilla, M. Fazzari, N. Srivastava, H. W. Yeung, J. L. Humm, J. Guillem, R. Downey, M. Karpeh, A. E. Cohen, and R. Ginsberg, "Tumor treatment response based on visual and quantitative changes in global tumor glycolysis using PET-FDG imaging. The visual response score and the change in total lesion glycolysis," *Clin Positron Imaging.* **2**(3), 159–171 (1999).
 - ²⁰U. Nestle *et al.*, "18F-Deoxyglucose positron emission tomography (18FDG-PET) for the planning of radiotherapy in lung cancer: High impact in patients with atelectasis," *Int. J. Radiat. Oncol., Biol., Phys.* **44**, 593–597 (1999).
 - ²¹A. C. Paulino and P. A. Johnstone, "FDG-PET in radiotherapy treatment planning: Pandora's box?," *Int. J. Radiat. Oncol., Biol., Phys.* **59**, 4–5 (2004).
 - ²²Y. E. Erdi, O. Mawlawi, S. M. Larson, M. Imbriaco, H. Yeung, R. Finn, and J. L. Humm, "Segmentation of lung lesion volume by adaptive positron emission tomography image thresholding," *Cancer* **80**, 2505–2509 (1997).
 - ²³Q. C. Black, I. S. Grills, L. L. Kestin, C. Y. O. Wong, J. W. Wong, A. A. Martinez, and D. Yan, "Defining a radiotherapy target with positron emission tomography," *Int. J. Radiat. Oncol., Biol., Phys.* **60**(4), 1272–1282 (2004).
 - ²⁴M. El-Bassiouni, I. F. Ciernik, J. B. Davis, I. El-Attar, B. Reiner, C. Burger, G. W. Goerres, and G. M. Studer, "[18FDG] PET-CT-based intensity-modulated radiotherapy treatment planning of head and neck cancer," *Int. J. Radiat. Oncol., Biol., Phys.* **69**(1), 286–293 (2007).
 - ²⁵L. Soma, M. Picchio, M. Gilardi, C. Messa, V. Bettinardi, M. Danna, R. Giovanna, I. Dell'Oca, S. Schipani, N. Di Muzio, and F. Fazio, "Thresholding segmentation of FDG PET lung lesions for RT planning purposes," *Int. J. Radiat. Oncol., Biol., Phys.* **63**(1), S403–S404 (2005).
 - ²⁶S. Jan, G. Santin, and D. Strul, "GATE: A simulation toolkit for PET and SPECT," *Phys. Med. Biol.* **49**, 4543–4561 (2004).
 - ²⁷C. R. Schmidlein, A. S. Kirov, S. A. Nehmeh, L. M. Bidaut, Y. E. Erdi, J. L. Humm, and H. I. Amols, "Validation of GATE Monte Carlo simulations of the GE Advance/Discovery LS PET scanners," *Med. Phys.* **33**(1), 198–208 (2006).
 - ²⁸K. Thielemans, S. Mustafovic, and C. Tsoumpas, "STIR: Software for tomographic image reconstruction release 2," *Nuclear Science Symposium Conference Record*, (IEEE, San Diego, 2006).
 - ²⁹C. Labbé *et al.*, "An object-oriented library for 3D PET reconstruction using parallel computing," in *Proceedings of Bildverarbeitung fuer die Medizin 1999, Algorithmen-Systeme-Anwendungen, Informatik Aktuell* (Springer, 1999), pp. 268–272.
 - ³⁰W. S. Rasband, IMAGEJ, National Institutes of Health, Bethesda, MD, (<http://rsb.info.nih.gov/ij/>), 1997–2004.
 - ³¹CURVEEEXPERT (<http://curveexpert.webhop.biz/>).
 - ³²J. Van de Steene, N. Linthout, J. de Mey, V. Vinh-Hung, C. Claassens, M. Noppen, A. Bel, and G. Storme, "Definition of gross tumor volume in lung cancer: Inter-observer variability," *Radiother. Oncol.* **62**(1), 37–49 (2002).